

Weighing Cosmic Structures with Clusters of Galaxies and the Intergalactic Medium

Matteo Esposito,^{1,2*} Vid Iršič,^{3,4} Matteo Costanzi,^{2,5,6} Stefano Borgani,^{2,5,6,7} Alexandro Saro,^{2,5,6,7}
Matteo Viel^{5,6,7,8}

¹*MPE - Max-Planck-Institut für extraterrestrische Physik, Postfach 1312, Giessenbachstr., 85741 Garching, Germany*

²*Astronomy Unit, Department of Physics, University of Trieste, via Tiepolo 11, I-34131 Trieste, Italy*

³*Kavli Institute for Cosmology, University of Cambridge, Madingley Road, Cambridge CB3 0HA, UK*

⁴*Cavendish Laboratory, University of Cambridge, 19 J. J. Thomson Ave., Cambridge CB3 0HE, UK*

⁵*IFPU - Institute for Fundamental Physics of the Universe, Via Beirut 2, 34014 Trieste, Italy*

⁶*INAF - Osservatorio Astronomico di Trieste, via G. B. Tiepolo 11, I-34143 Trieste, Italy*

⁷*INFN - Sezione di Trieste, Trieste, Italy*

⁸*SISSA, Via Bonomea 265, 34136 Trieste, Italy*

Accepted XXX. Received YYY; in original form ZZZ

ABSTRACT

We present an analysis aimed at combining cosmological constraints from number counts of galaxy clusters identified through the Sunyaev-Zeldovich effect, obtained with the South Pole Telescope (SPT), and from Lyman- α spectra obtained with the MIKE/HIRES and X-shooter spectrographs. The SPT cluster analysis relies on mass calibration based on weak lensing measurements, while the Lyman- α analysis is built over mock spectra extracted from hydrodynamical simulations. The resulting constraints exhibit a tension ($\sim 3.3\sigma$) between the low σ_8 values preferred by the low-redshift cluster data, $\sigma_8 = 0.74^{+0.03}_{-0.04}$, and the higher one preferred by the high-redshift Lyman- α data, $\sigma_8 = 0.91^{+0.03}_{-0.03}$. We present a detailed analysis to understand the origin of this tension and to establish whether it arises from systematic uncertainties related to the assumptions underlying the analyses of cluster counts and/or Lyman- α forest. We found this tension to be robust with respect to the choice of modelling of the IGM, even when including possible systematics from unaccounted sub-Damped Lyman- α (DLA) and Lyman-limit systems (LLS) in the Lyman- α data. We conclude that to solve this tension would require a large bias on the cluster mass estimate, or large unaccounted errors on the Lyman- α mean fluxes. Our results have important implications for future analyses based on cluster number counts from future large photometric surveys (e.g. Euclid and LSST) and on larger samples of high-redshift quasar spectra (e.g. DESI and WEAVE surveys). If confirmed at the much higher statistical significance reachable by such surveys, this tension could represent a significant challenge for the standard Λ CDM paradigm.

Key words: Cosmology: large-scale structure of Universe – Galaxies: clusters, intergalactic medium – Methods: numerical

1 INTRODUCTION

In the last decades, a variety of probes of the large-scale structure (LSS) of the Universe have been widely used to study fundamental cosmology, reaching now competitive constraints with respect to other classical cosmological probes like the Cosmic Microwave Background (CMB) (DES Collaboration et al. 2021; Alam et al. 2021; Heymans et al. 2021, and references therein). Among all the LSS probes, galaxy clusters and the intergalactic medium (IGM) are of particular interest in the context of cosmology, given their complementarity in terms of both redshift range and overdensity range probed. Indeed, at $z \lesssim 1.5$ galaxy clusters mark the largest cosmic perturbations that evolved in the non-linear regime and reached virial equilibrium. On the other hand, the Lyman- α forest traces at

$2 \lesssim z \lesssim 6$ structures over a wide range of scales which are still in the quasi-linear or mildly non-linear regime.

More precisely, the galaxy clusters number density evolution can be used to infer cosmological models by comparing the expected number of clusters of a certain mass and at a certain time obtained with semi-analytical methods, with the observed counts. Together with their detection, the mass determination of the clusters of galaxies is then of paramount importance for cluster cosmology. However, the techniques used to "weigh" these clusters individually are either observationally very expensive or not very accurate. Especially when dealing with large cluster surveys, it is not possible to apply the former on each of the detected objects and thus one often relies on the scaling relations that link the observable on which the survey is based to the cluster mass. Since the cluster mass calibration is the main limitation in current surveys, it is then of fundamental importance to understand the possible biases and uncertainties of

* esposito@mpe.mpg.de

such mass-observable relations as they can alter the cosmological parameter constraints. For this reason a lot of effort has been put into their calibration and refinement in the last years (see e.g. [Allen et al. 2011](#); [Kravtsov & Borgani 2012](#) for reviews on cluster cosmology). Among the different observables used to construct cluster surveys, the thermal Sunyaev-Zel'dovich effect (SZ, [Sunyaev & Zeldovich 1970](#))¹, has a twofold advantage: firstly, the SZ signal is independent of cluster redshifts; secondly, it is proportional to the (line-of-sight integrated) pressure of the intra-cluster plasma, a quantity closely linked to cluster mass through hydrostatic equilibrium. For this reason, in the last years many sub-millimeter-wave surveys (ACT, SPT, Planck; see e.g. [Bleem et al. 2015](#); [Planck Collaboration 2016](#); [Hilton et al. 2018](#)) have been used to construct cluster catalogs to be used to constrain cosmological parameters.

Similarly, the IGM has been widely studied in the last decades thanks to the development of ever improving semi-analytical and numerical models. Its main manifestation, the Lyman- α forest, is a feature in the spectra of high redshift quasars consisting of a series of absorption lines, which can be used to track the distribution of neutral hydrogen along the line of sight. Hydrodynamical simulations are nowadays accurate enough to produce reliable mock spectra of the Lyman- α forest for cosmological studies. However, the observational properties of the Lyman- α forest also depend on the IGM thermal history and thus this must also be varied, along with cosmological parameters, in order to explore all the possible scenarios. More precisely, the effects of varying the thermal state of the IGM can mimic, at small scales, that induced by variations in the cosmological parameters; the resulting degeneracy between cosmology and IGM thermal history leads to looser constraints on cosmological parameters. In the last years, large surveys of low-resolution and low signal-to-noise quasars spectra (SDSS, BOSS, see e.g. [McDonald et al. 2005](#); [Palanque-Delabrouille et al. 2013](#); [Chabanier et al. 2019](#); [Palanque-Delabrouille et al. 2020](#)) as well as moderate size samples with tens of high signal-to-noise and high-resolution spectra (VLT, HIRES/KECK, see e.g. [Viel et al. 2004](#); [Viel et al. 2013a](#); [Iršič et al. 2017](#); [Boera et al. 2019](#); [Walther et al. 2019](#); [Karaçaylı et al. 2021](#)) have been used to constrain the structure formation cosmological parameters on scales of 0.1 - 10 Mpc/h (see e.g. [McQuinn 2016](#) for a review on IGM).

Combining the Lyman- α spectra with the cluster number counts can help improving the parameter inference by breaking the degeneracies between different parameters in each data set (see [Costanzi et al. 2014](#) for a previous attempt at combining these two probes). As mentioned, we expect this particular combination to be effective in view of the complementarity of clusters and Lyman- α forest both in redshift ranges and dynamical regimes covered: while clusters of galaxies are highly dense (typically about 200 times denser than the average density of the Universe, up to their outer radius) and large structures observed at low or intermediate redshifts ($z \sim 0 - 2$), the quasars that show a Lyman- α forest can be found at much higher redshifts ($z \sim 2 - 5$) and the hydrogen that is responsible for the absorption lines trace much lower densities ($\lesssim 10$ times denser than the average density of the Universe). Another interesting synergy between clusters and IGM is provided by investigations in which the thermal evolution of the cosmic web is followed down to small redshifts allowing for some pre-heating of the IGM, as in [Borgani & Viel \(2009\)](#).

This paper aims at exploiting such complementarity and in partic-

ular at investigating the compatibility of two recent analyses that use galaxy clusters and the Lyman- α flux power spectrum for cosmological parameter inference: the work of [Bocquet et al. \(2019\)](#) which uses number counts of clusters detected by the South Pole Telescope (SPT) through the Sunyaev-Zel'dovich (SZ) effect, and that of [Iršič et al. \(2017\)](#) which studies Lyman- α forest spectra obtained with the Very Large Telescope (VLT) and the Keck and Magellan telescopes. These two analyses rely on high quality data as well as sophisticated state-of-the-art analytical and numerical methods. Therefore, their comparison acts as a test of the predictions of the standard Λ CDM model on cosmic growth over a wide redshift range, while their combination has the potential to provide tight constraints on cosmological parameters. On the other hand, a possible tension between such two probes could point toward the existence of unveiled systematics in the analysis methods or even the need of extensions of the standard cosmological model.

Both the Lyman- α spectra and the cluster number counts can constrain the late-time amplitude of the matter power spectrum, here parametrized with σ_8 , with past works having shown that the former typically prefers somewhat higher values for this parameter - with respect e.g. to the Planck results ([Planck Collaboration 2020](#)) - while the latter usually prefer lower ones. The purpose of the analysis presented in this paper is in fact to carry out an updated analysis of recent data on cluster number counts and Lyman- α data to assess whether such a tension persists and, in that case, quantify its significance and attempt to trace its origin.

The structure of the paper can be summarized as follows. We describe in § 2 the observational data sets used for cluster number counts and Lyman- α data, and the numerical simulations used for the cosmological exploitation of the latter. In § 3 we present the methods of analysis and discuss the resulting cosmological constraints in § 4. Finally, we comment such results and provide our conclusions in § 5.

2 DATA AND SIMULATIONS

2.1 Lyman- α forest: XQ-100, MIKE, HIRES

The Lyman- α analysis relies on two different and complementary data sets: the XQ-100 sample ([López, S. et al. 2016](#); [Iršič et al. 2016](#)), which provides 100 medium resolution ($R \approx 5000$) and signal-to-noise ($S/N \approx 30$) spectra and the HIRES/MIKE sample ([Viel et al. 2013a](#)), consisting of 25 high resolution ($R \approx 80000$) and high signal-to-noise ($S/N > 80$) spectra.

XQ-100 sample: We used 100 QSO spectra from the XQ-100 Legacy Survey, observed with the X-Shooter spectrograph on the Very Large Telescope (VLT). These are medium resolution and signal-to-noise spectra with emission redshifts $3.5 < z_{\text{em}} < 4.5$. The main quantity extracted from these data is the flux power spectrum, P_F , i.e. the power spectrum of the overdensity of the normalized flux of the quasar, along the line of sight (see e.g. [McQuinn 2016](#)). Its extraction from the QSO spectra is modeled with the help of mock data from hydrodynamic simulations, allowing an accurate estimation of the flux power at $z = 3, 3.2, 3.4, 3.6, 3.8, 4, 4.2$ for 19 linearly separated k -bins in the range $0.003 - 0.057 \text{ s km}^{-1}$. The value of the P_F is thus available for a total of 133 points in the (k, z) space. The errors and correlations between the values of the P_F are summarized in the covariance matrix, which is obtained through the use of the bootstrap method. However, in order to correct for the underestimation of the variance due to the limited number of sightlines used (see e.g. [Rollinde et al. 2012](#); [Iršič et al. 2013](#); [Iršič et al. 2017](#); [Wilson](#)

¹ The SZ signal arises from the scatter of the CMB photons off the hot electrons of the intracluster medium (ICM)

et al. 2021), we multiplied the full matrix by a factor of 1.3, which has been obtained by a comparison of different methods for estimation of the covariance matrix. We refer to López, S. et al. (2016) for further details on the data and to Iršič et al. (2016) for the flux power spectrum extraction.

HIRES/MIKE sample: This sample consists of 25 high-resolution QSO spectra with emission redshifts $4.5 < z_{\text{em}} < 6.5$. For 14 of the observed objects, the spectra were taken with the Keck High Resolution Echelle Spectrometer (HIRES), while the remaining 11 were taken with the Magellan Inamori Kyocera Echelle (MIKE) spectrograph on the Magellan Clay telescope. For both data sets, the measured P_F is available at $z = 4.2, 4.6, 5.0, 5.4^2$ for 7 linearly separated $\log k$ -bins in the range $0.005 - 0.079 \text{ s km}^{-1}$ resulting in a total of 49 data points. Following Viel et al. (2013a), similarly to what we did for the XQ-100 data set, we used a correction factor of 1.5 for the covariance matrix of the flux power spectrum. A detailed description of this data set can be found in Viel et al. (2013a).

Simulations: Along with observational data, a set of simulations is used in the analysis (based on Sherwood simulations - Bolton et al. 2016; details in Iršič et al. 2017). These simulations were performed with the GADGET-3 code, an updated version of the publicly available GADGET-2 code (Springel 2005). Besides radiative cooling and the effect of a redshift dependent UV background, a simple star formation criteria is used, converting gas particles above an overdensity 1000 and with a temperature below 10^5 K into stars (i.e. collisionless particles).

The reference model simulation is a box with 2×768^3 gas and dark matter particles and a box size of $20/h$ comoving Mpc, in a flat Λ CDM universe with $\Omega_{m,0} = 0.301$, $\Omega_{b,0} = 0.0457$, $n_s = 0.961$, $H_0 = 70.2 \text{ km s}^{-1}$ and $\sigma_8 = 0.829$. When using the flux power spectrum to constrain cosmological parameters, one can exploit the fact that they impact on it through the amplitude and slope of the matter power spectrum, $P_m(k)$ at the scales probed by the Lyman- α forest (McDonald et al. 2005; Iršič et al. 2017; Pedersen et al. 2021). Therefore, we chose to use the amplitude of the late time matter power spectrum, σ_8 , and its effective slope, $n_{\text{eff}} = d \ln P_m(k) / d \ln k$, evaluated at $k = 0.005 \text{ s km}^{-1}$, as the parameters that describe our cosmological models. In order to sample different cosmologies, simulations have been run for five different values of both $\sigma_8 = 0.754, 0.804, 0.829, 0.854, 0.904$ and $n_{\text{eff}} = -2.3474, -2.3274, -2.3074, -2.2874, -2.2674$.

As for the thermal history of the IGM, its effect is treated by modifying the background photo-heating rates to tune the simulations to different values for the temperature at mean density $T_0(z = 3.6) = 7200, 11000, 14800 \text{ K}$ and the slope $\gamma(z = 3.6) = 1.0, 1.3, 1.5$ of the temperature-density relation of the low density IGM: $T = T_0(1 + \delta)^{\gamma-1}$. These calculations are based on the Haardt & Madau (2012) model for a ionising uniform UV background. The cooling model takes into account various processes as collisional excitation cooling, bremsstrahlung cooling and inverse Compton cooling off CMB photons, but do not include line cooling as these are expected to have low impact on the Lyman- α forest spectra (Viel et al. 2013b). For the same reason, galactic winds and AGN feedback are also not considered in the simulations.

To account for possible spatial fluctuations in the UV ionising

² The $P_F(k, z)$ at $z = 5.4$ is only available for the HIRES sample as the corresponding redshift bin in the MIKE data set has a very low number of sightlines.

| Parameter | Values |
|----------------------------|---|
| σ_8 | [0.754, 0.804, 0.829, 0.854, 0.904] |
| n_{eff} | [-2.3474, -2.3274, -2.3074, -2.2874, -2.2674] |
| $T_0(z = 3.6) \text{ [K]}$ | [7200, 11000, 14800] |
| $\gamma(z = 3.6)$ | [1.0, 1.3, 1.5] |
| f_{QSO} | [0, 0.5, 1.0] |
| z_{rei} | [7, 9, 15] |

Table 1. Summary of the parameters varied in the simulation suite used for the Lyman- α analysis. The mean flux parameters are not listed here because they are varied in the post-processing when extracting the mock spectra and not in the simulations. These are varied by a multiplicative factor of [0.3 - 1.5] around the reference model of Palanque-Delabrouille et al. (2013)

background at high redshift, an inhomogeneous flux component arising from a rare QSO population is inserted into the simulations. This is obtained by identifying halos with a friend-of-friend algorithm and assigning them a luminosity given by the QSO luminosity function. Then a ionising flux bubble is computed from each of the identified halos. See Bolton & Viel (2011) and the appendix in Viel et al. (2013a) for details on the method. In our analysis the effect of UV fluctuations is parametrized in terms of $f_{\text{QSO}} = 0, 0.5, 1$, defined as the fraction of volume averaged hydrogen photo-ionisation rate arising from a fluctuating QSO component.

For each simulation, we also varied the mean transmitted flux $\langle F \rangle$, by rescaling the optical depth ($\tau_{\text{eff}} = -\ln \langle F \rangle$) to the observed values with some bias: $\tau_{\text{eff}} = f \cdot \tau_{\text{obs,eff}}$ with $f \in [0.3, 1.5]$ and $\tau_{\text{obs,eff}}$ being the measurements of Palanque-Delabrouille et al. (2013). Note that the variation of the mean flux is a post-processing procedure aimed at capturing the uncertainty in the photo-ionization rate, and does not require other simulations.

Finally, the redshift of reionization is also varied in the simulations with $z_{\text{rei}} = 7, 9, 15$. This is not well constrained by our data, but has an impact on the thermal history of the IGM, so it is important to marginalize over it.

A summary of the parameters varied in the simulations is shown in table 1. Each parameter has been varied once at a time with the exception of the thermal state parameters, T_0 and γ which are varied in a 3×3 grid to include all the possible 9 combinations. This in turn gives 1 reference model, 4 models varying σ_8 , 4 models varying n_{eff} , 8 models varying the thermal state parameters, 2 models varying z_{rei} and 2 models varying f_{QSO} , for a total of 21 models.

2.2 Galaxy clusters: SPT-SZ, WL masses

The cluster sample is made of 343 clusters identified through the Sunyaev-Zeldovich effect from the 2500 deg^2 SPT-SZ survey, which have been optically confirmed and have redshift measurements (Bleem et al. 2015). Mass estimates rely on weak lensing shear profiles obtained for 19 clusters by the Magellan/Megacam imager and for 13 clusters by the Hubble Space Telescope (Dietrich et al. 2019; Schrabback et al. 2018).

The SZ selected cluster sample: The SPT-SZ survey is provided by the South Pole Telescope (SPT) observing the sky in three millimeter wavebands centered at 95, 150 and 220 GHz. It has a field of view of ~ 1 degree and a resolution of ~ 1 arcmin, which allows deeper observations than those obtained with satellites used for all-sky maps (WMAP, Planck); this makes it well suited for the detection of high-mass clusters through the SZ-effect from $z \geq 0.2$ up to the highest

redshifts at which clusters exist. The survey spans a contiguous 2500 deg^2 area within the boundaries $20\text{h} \leq \text{R.A.} \leq 7\text{h}$ and $-65^\circ \leq \text{Dec.} \leq -40^\circ$.

The cluster extraction procedure (see [Williamson et al. 2011](#) for details) uses a map-matching filter to discriminate the cluster SZ signal from spurious effects due to atmospheric/instrumental and astrophysical noise. The maps were filtered at 12 different cluster scales, varying the reference radii of the adopted spherical model; following the approach of [Vanderlinde et al. \(2010\)](#) the detection significance ξ , used as the primary SZ observable, is defined as the highest signal-to-noise value associated with a decrement in the SZ map, across all filter scales.

The cluster sample used in this work consists of 343 clusters extracted from the full SPT-SZ catalogue presented in [Bleem et al. \(2015\)](#) for which redshift measurements are available and restricted to $z > 0.25$ and $\xi > 5$, achieving an expected and measured purity of 95 per cent.

WL mass estimates: We exploit in the analysis WL shear measurements for 32 clusters: 19 of these were observed with the Megacam imager mounted on the Magellan Clay telescope, spanning the redshift range $0.29 \leq z \leq 0.69$ ([Dietrich et al. 2019](#)), while the remaining 13 at redshifts $0.576 \leq z \leq 1.132$ were observed with the Advanced Camera for Surveys on the Hubble Space Telescope ([Schrabback et al. 2018](#)). The data used in our analysis are the reduced tangential shear profiles and the estimated redshift distribution of the source galaxies. Details on the data reduction and analysis can be found in the aforementioned works.

3 ANALYSIS AND METHODS

3.1 Cosmological parameters

Our analysis is performed through `CosmoSIS` ([Zuntz et al. 2015](#)), a code for cosmological parameter estimation that allows one to combine different data sets, taking advantage of its modularity. In order to compare the cosmological constraints to be obtained from the Lyman- α analysis to those to be derived from the SPT cluster number counts, for both analyses we sampled the full $\nu\Lambda\text{CDM}$ cosmological parameter space: $(A_s, n_s, \Omega_{m,0}, \Omega_{b,0}h^2, \Omega_{\nu,0}h^2, h, \tau)$. Here A_s is the amplitude of the linear matter power spectrum, n_s the primordial spectral index, $\Omega_{m,0}$, $\Omega_{b,0}$ and $\Omega_{\nu,0}$ the values at the present time for the density parameters associate to the total matter content, baryons and massive neutrinos, respectively, while h is the Hubble constant in units of $100 \text{ km s}^{-1} \text{ Mpc}^{-1}$. Based on these parameters, at each step in both analyses we included a `CAMB` ([Lewis et al. 2000](#)) `CosmoSIS` module, to retrieve the linear matter power spectrum and use it for the evaluation of the expected cluster number density and for calculating its amplitude (σ_8) and effective slope (n_{eff}) which enter the Lyman- α likelihood.

3.2 Lyman- α forest

In order to perform our analysis with the help of `CosmoSIS`, we wrote a `CosmoSIS` module based on the same data and likelihood presented in [Iršič et al. \(2017\)](#) (henceforth [I17](#)). As a first check, we verified that results obtained using our `CosmoSIS` module are fully consistent with those originally obtained by [I17](#). A short presentation of such comparison can be found in appendix [A](#).

The cornerstone of the pipeline is the likelihood evaluation for the simulated model. The likelihood function we used is a simple

Gaussian multi-variate, which is computed by comparing the simulated flux power spectra, $P_F(k, z)$, for a given set of parameters, with the observed ones. The expected values are obtained through interpolation between points of the available simulations grid in the parameter space (see § 2.1). According to [I17](#) the interpolation error is small ($< 5\%$) and does not contribute much to the total error budget of the current data. In fact, it does not bias the results and is thus ignored in our analysis. It is however important to notice that this upper bound on the interpolation error has been tested only in the explored parameter space. This may not be the case if extrapolation out of the parameter space occurs (see the comment on the constraint on n_{eff} in § 4.1).

The cosmological simulations employed are labelled by three redshift-dependent parameters $(\gamma, T_0, \langle F \rangle)$, see § 2.1 which can be modelled, in our analysis pipeline, as power-laws of $(1+z)$ or by assigning to each of them independent values within each redshift, eventually setting a maximum difference between the values taken at adjacent bins. In all the analyses presented here, unless otherwise specified, we used independent values within each of the 10 redshift bins for the mean flux $\langle F \rangle$, while we assume power-laws of $(1+z)$ for the amplitude T_0 and the slope γ of the IGM equation of state:

$$\begin{aligned} T_0(z) &= T_0^A [(1+z)/(1+z_p)]^{T_0^S}; \\ \gamma(z) &= \gamma^A [(1+z)/(1+z_p)]^{\gamma^S}, \end{aligned} \quad (1)$$

where the superscripts A and S refer to the amplitude and slope of the power-law relation and z_p is the redshift pivot, here set to $z_p = 4.2$.

Given its impact on the IGM thermal history, in our analysis we also varied the redshift of reionization z_{rei} . However, this parameter does depend on one of the employed cosmological parameters: the optical depth at recombination τ . Moreover, z_{rei} is also weakly correlated with the temperature at mean density of the IGM, T_0 . Hence, we modelled these two dependencies in order to reduce the sampled parameter space and map them one to another. Looking at our simulations, we have found that linearly interpolating the $z_{\text{rei}} - \tau$ and $z_{\text{rei}} - T_0$ relations independently, results in these parametrization:

$$\tau = 0.098 z_{\text{rei}} - 0.022 \quad (2)$$

$$\tau = 0.001 T_0 + 0.065. \quad (3)$$

Here, T_0 is evaluated at the pivot redshift z_p and is given in units of 10^4 K . The above dependence on T_0 is very weak and for this reason we ignored it in our analysis, simply mapping $\tau \leftrightarrow z_{\text{rei}}$. Even though τ does not have any impact on the SPT analysis, we decided to include in our module the mapping to this CMB parameter in order to have a consistent framework for future analyses that may include CMB data.

Hence, the fully sampled parameter space is made of: 10 parameters for the average flux $\langle F \rangle$ (one for each redshift bin), 2 parameters for each power-law (T_0 and γ), one parameter describing the non-uniform component of the ionizing background (f_{QSO}) and 7 cosmological parameters of the $\nu\Lambda\text{CDM}$ model ($A_s, n_s, \Omega_{m,0}, \Omega_{b,0}h^2, \Omega_{\nu,0}h^2, h, \tau$), for a total of 22 parameters.

3.3 Galaxy clusters

The galaxy clusters analysis is performed by following the same procedure as [Bocquet et al. \(2019\)](#) (henceforth [B19](#)), as we used their - publicly available - `CosmoSIS` module. Thus, we only briefly present here the mass proxies used, as well as the results of the analysis, while the reader interested in the details of the methods used can refer to their paper.

3.3.1 Mass calibration

To calibrate the detection significance, ξ , the SPT mass proxy, [Bocquet et al. \(2019\)](#) relied on high quality WL follow-up data.

To account for the impact of noise bias in the measurement of the SZ effect, we characterize the SZ signal with ζ , the detection signal-to-noise ratio (SNR) at the true underlying cluster position and filter scale. This quantity has been shown to be related to the detection significance ξ through a Gaussian distribution with unit scatter and mean $\langle \xi \rangle = \sqrt{\zeta^2 + 3}$ ([Vanderlinde et al. 2010](#)). We parametrize the ζ -mass relation as

$$\langle \ln \zeta \rangle = \ln A_{SZ} + B_{SZ} \ln \left(\frac{M_{500} h_{70}}{4.3 \times 10^{14} M_{\odot}} \right) + C_{SZ} \ln \left(\frac{E(z)}{E(0.6)} \right), \quad (4)$$

where $h_{70} = H_0/100/0.7$. For the WL mass calibration, a bias parameter, b_{WL} , is also introduced, so that the relationship between actual cluster mass, M_{500} , and its weak-lensing estimate, M_{WL} , reads

$$\langle \ln M_{WL} \rangle = \ln b_{WL} + \ln M_{500}. \quad (5)$$

In the above equations, the redshift and mass dependencies are given in terms of the dimensionless Hubble parameter $E(z)$ and the mass, M_{500} , which is defined as the total mass contained within a sphere encompassing a mean overdensity 500 times the critical one. Brackets indicate the expected values for the scaling relations that are assumed to have an intrinsic Gaussian scatter with widths $\sigma_{\ln \zeta}$ and σ_{WL} . We also allow for correlated scatter between the SZ and WL mass proxies, with all such correlation coefficients being varied along with cosmological parameters.

Equation 5 introduces a bias parameter for the WL mass estimate. This bias accounts for systematic errors in the mass modelling or to systematics in the measurements. The latter are in general related to the instruments and can in principle be different for data obtained with different telescopes/instruments, in our case Magellan/Megacam and HST. In order to take into account such uncertainties, the WL bias can be modelled as

$$b_{WL,i} = b_{WL, \text{mass},i} + \delta_{WL, \text{bias}} \Delta b_{WL, \text{mass model},i} + \delta_i \Delta b_{\text{sys},i} \quad (6)$$

with $i \in \{\text{Megacam, HST}\}$.

In the above equation $b_{WL, \text{mass model}}$ is the mean bias due to mass modelling; $\Delta b_{WL, \text{mass model}}$ is the associated uncertainty and Δb_{sys} is the systematic measurement uncertainty. Here, $\delta_{WL, \text{bias}}$, δ_{Megacam} and δ_{HST} are free parameters that we vary in our analysis. At the same time, we model the intrinsic scatter of the mass-observable relations (MOR) due to the fitting of the shear profiles against NFW profiles as

$$\sigma_{WL,i} = \sigma_{\text{intrinsic},i} + \delta_{WL, \text{scatter}} \Delta \sigma_{\text{intrinsic},i} \quad (7)$$

with $i \in \{\text{Megacam, HST}\}$.

Moreover, the intervening large-scale structures can distort the WL shear signal by causing additional deflection of the lensed images and resulting in an error in the cluster mass determination. We model this scatter by following the same approach used above:

$$\sigma_{WL, \text{LSS},i} = \sigma_{\text{LSS},i} + \delta_{\text{LSS},i} \Delta \sigma_{\text{LSS},i} \quad (8)$$

with $i \in \{\text{Megacam, HST}\}$,

where again $\sigma_{\text{intrinsic}}$ and σ_{LSS} are the values of the mean scatter associated to the lensing signal of the cluster and of the large-scale

structure, respectively; $\Delta \sigma_{\text{intrinsic}}$ and $\Delta \sigma_{\text{LSS}}$ are the corresponding errors on such means; $\delta_{WL, \text{scatter}}$, $\delta_{\text{LSS}, \text{Megacam}}$ and $\delta_{\text{LSS}, \text{HST}}$ are the free parameters, describing the multiplicative telescope noise, which are varied in the chains. The WL modelling framework is described in detail by [Dietrich et al. \(2019\)](#), while estimates of the modelling parameters introduced in the above equations can be found in Table 1 of [B19](#). Through these relations, the observables can be related to the mass of the galaxy clusters which in turn can be linked to the redshift- and mass-dependent HMF.

The adopted fitting model for the HMF is that of [Tinker et al. \(2008\)](#),

$$n(M, z) = \frac{\bar{\rho}}{M} A \left[\left(\frac{\sigma_M}{b} \right)^{-a} + 1 \right] e^{-c/\sigma_M^2} \left| \frac{d \ln \sigma_M}{dM} \right|, \quad (9)$$

where $\bar{\rho}$ is the average density of the Universe, σ_M is the variance of the density field calculated on spheres that enclose a mass M and A, a, b, c are the fitting parameters which were calibrated against N-body simulations. The Tinker HMF is strongly dependent on the overdensity Δ used for determining the mass of the simulated clusters, that in the analysis by [Tinker et al. \(2008\)](#) were detected by applying a SO algorithm. In particular, this HMF is calibrated in the range $200 \leq \Delta_{\text{mean}} \leq 3200$ where Δ_{mean} is the overdensity with respect to the mean background density. Since we are working with overdensities of 500 with respect to the critical density, the mean spherical overdensity is obtained through $\Delta_{\text{mean}}(z) = 500/\Omega_m(z)$.

Based on the simultaneous fit of the mass-observable relations and of the HMF model, the galaxy cluster analysis relies on a multi-observable Poisson log-likelihood. With some algebraic modifications (for details see sec. 3.2 of [B19](#)) this takes the form:

$$\ln \mathcal{L}(\theta) = \sum_i \ln \left. \frac{dN(\xi, z|\theta)}{d\xi dz} \right|_{\xi_i, z_i} - \int_{z_{\text{cut}}}^{\infty} dz \int_{\xi_{\text{cut}}}^{\infty} d\xi \left[\frac{dN(\xi, z|\theta)}{d\xi dz} \right] + \sum_j \ln P(g_t | \xi_j, z_j, \theta)_{g_{t_j}}. \quad (10)$$

where the first sum runs over all clusters i in the survey and the second one over all clusters j for which follow-up WL tangential shear, g_t , measurements are available. Such form explicitly separates the contribution to the likelihood from the SZ clusters abundance (the first two terms) and from the mass calibration measurements (the third term). The two integrals of the second term are truncated by the survey selection function and more precisely with $\xi_{\text{cut}} = 5$ and $z_{\text{cut}} = 0.25$. We refer to sec. 3.2 of [B19](#) for details on the definition of the likelihood and how each term is computed.

4 RESULTS

Using the data sets presented in § 2 and encoded in the `CosmosIS` modules presented in § 3, we derived posteriors on the relevant parameters by carrying out the analyses of the Lyman- α and SPT cluster number counts separately. The exploration of the parameter space has been carried out using `MULTINEST`³ ([Feroz et al. 2009](#)), a multi-modal nested sampler (see e.g. [Skilling 2004](#) for a description of nested sampling) which exploits sophisticated proposal algorithms to efficiently sample multi-modal distributions.

We present in this section the results of the Lyman- α analysis and

³ <https://github.com/farhanferoz/MultiNest>

| Parameter | Prior | Parameter | Prior |
|------------------------------|----------------------------|------------------------------|----------------------------|
| f_{QSO} | $\mathcal{U}(0, 1)$ | $\langle F \rangle(z = 3.4)$ | $\mathcal{N}(0.562, 0.04)$ |
| z_{rei} | $\mathcal{U}(7, 15)$ | $\langle F \rangle(z = 3.6)$ | $\mathcal{N}(0.519, 0.04)$ |
| T_0^S | $\mathcal{U}(-5, 5)$ | $\langle F \rangle(z = 3.8)$ | $\mathcal{N}(0.467, 0.04)$ |
| T_0^A | $\mathcal{U}(0.3, 2)$ | $\langle F \rangle(z = 4.0)$ | $\mathcal{N}(0.419, 0.04)$ |
| γ^S | $\mathcal{U}(-5, 5)$ | $\langle F \rangle(z = 4.2)$ | $\mathcal{N}(0.364, 0.04)$ |
| γ^A | $\mathcal{U}(0, 2)$ | $\langle F \rangle(z = 4.6)$ | $\mathcal{N}(0.30, 0.04)$ |
| $\langle F \rangle(z = 3.0)$ | $\mathcal{N}(0.681, 0.04)$ | $\langle F \rangle(z = 5.0)$ | $\mathcal{N}(0.18, 0.04)$ |
| $\langle F \rangle(z = 3.2)$ | $\mathcal{N}(0.625, 0.04)$ | $\langle F \rangle(z = 5.4)$ | $\mathcal{N}(0.08, 0.04)$ |

Table 2. Priors for the astrophysical parameters used in the Lyman- α analysis. Each of the $\langle F \rangle(z)$ parameters also has a flat prior in the range (0, 1). The prior on z_{rei} reflects the boundaries of the available simulations and that on T_0^A poses a physical limit on the thermal history of the IGM. A tighter prior is set manually on γ , such that $1 < \gamma(z) < 1.7$ at each redshift bin.

of the SPT analysis, at first separately. For these two analysis, we show the best-fit models in fig. 1 and fig. 2, respectively. While we already anticipate some discussion on the posteriors obtained with the two analyses in two separate subsections, their contour plots are shown jointly in fig. 3.

All the constraints on parameters and contour plots shown in this section have been obtained using GetDist⁴ (Lewis 2019), a Gaussian kernel density estimator that takes the weighted MCMC chains and uses them to produce marginalized histograms to easily visualize the posterior. Unless otherwise stated, the multi-dimensional posterior plots always show the 68 per cent and 95 per cent contours of iso-confidence level.

4.1 Lyman- α forest

For our reference Lyman- α analysis we used the same priors on astrophysical parameters as those used by I17. In particular, Gaussian priors are used on $\langle F \rangle(z)$ for each redshift bin, centered on the values obtained in Palanque-DeLaBrouille et al. (2013) and with a standard deviation of 0.04, such that the results are not dominated by the prior. Wide, non-informative priors are set for the remaining parameters, with the exception of γ . For this parameter, a flat prior is set over the full redshift range in order to restrict it to physically plausible values. The parameters varied and their priors for the reference case are summarized in table 2. Here, and in all the tables henceforth, $\mathcal{U}(\text{min}, \text{max})$ denotes the uniform distribution between min and max , while the normal distribution with mean μ and standard deviation σ is indicated by $\mathcal{N}(\mu, \sigma)$.

We have also set priors on the cosmological parameters and these priors are shared by the two analyses. In particular, we have set Gaussian priors on those parameters that are constrained neither by the Lyman- α spectra, nor by the cluster number counts, namely $\Omega_{b,0}h^2$, $\Omega_{\nu,0}h^2$ and h . Such priors correspond to the marginalized posteriors obtained from CMB data in Planck Collaboration (2020), but with twice as large standard deviation. As for $\Omega_{\nu,0}h^2$, we used a Gaussian prior centered on the minimum value allowed by oscillation experiments (de Salas et al. 2018), with a reasonably large width to allow for deviations from it. On the remaining cosmological parameters, we have set flat uninformative priors which are listed in table 3 along with the aforementioned Gaussian priors.

The constraints obtained with such priors are shown as red contours in fig. 3 (see below for a discussion on the comparison to the

| Parameter | Prior |
|---------------------|---|
| n_s | $\mathcal{U}(0.94, 1)$ |
| A_s | $\mathcal{U}(10^{-10}, 10^{-8})$ |
| $\Omega_{m,0}$ | $\mathcal{U}(0.1, 0.6)$ |
| $\Omega_{b,0}h^2$ | $\mathcal{U}(0.02, 0.024) \times \mathcal{N}(0.02242, 0.00028)$ |
| $\Omega_{\nu,0}h^2$ | $\mathcal{U}(0, 0.01) \times \mathcal{N}(0.0006, 0.0002)$ |
| h | $\mathcal{U}(0.55, 0.9) \times \mathcal{N}(0.6766, 0.0084)$ |

Table 3. Priors on the cosmological parameters shared by the Lyman- α analysis and the SPT cluster number counts analysis. The Gaussian priors are taken from the results of Planck Collaboration (2020), by doubling their reported standard deviations. The prior on $\Omega_{\nu,0}h^2$ is centered on the minimum value allowed by neutrino oscillation experiments. The last column lists the values used when fixing the parameters.

galaxy cluster analysis results). As expected, our Lyman- α data can provide interesting constraints on σ_8 and n_{eff} . Such parameters are a combination of A_s , n_s and $\Omega_{m,0}$, which thus exhibit a strong correlation among each other. We have tried using different priors on the cosmological parameters and in particular we confirm that we retrieve the one-to-one mapping between $A_s - \sigma_8$ and $n_s - n_{\text{eff}}$ when all the other cosmological parameters are fixed. On the other hand, since we constrain directly σ_8 , when A_s , n_s and $\Omega_{m,0}$ are free to vary we see no much degeneracy with any of these parameters. The best-fit parameters provide a good fit to the data with a $\chi^2 = 181.48$ for 173 degrees of freedom (*d.o.f.*). This is also shown in fig. 1, where we plot the simulated flux power spectrum against the data, at different redshifts.

The constraints on n_{eff} show that part of the explored parameter space along that direction extends outside of the range covered by the simulations. In order to obtain prediction for those values of n_{eff} we resort to linear extrapolation. This might introduce an error larger than the one estimated for the interpolation scheme ($< 5\%$) and could indeed produce biased results. However, we do not expect any large impact in the σ_8 constraints given that the correlation between these two parameters is present, but not very large. Nonetheless, future work may want to explore this by running hydrodynamical simulations covering a larger range of n_{eff} .

As mentioned above, our reference analysis uses a power-law to parametrize the evolution of the IGM temperature at mean density, T_0 . In order to allow for more freedom in the IGM thermal history, we also ran an analysis with independent T_0 values at each redshift bin. We have ran two chains with and without informative priors and in every case we have found consistent contours for the cosmological parameters, showing that those constraints are robust with respect to the redshift evolution of T_0 .

4.2 Galaxy clusters

For our reference analysis of the number counts of SPT clusters, we used the same cosmological priors as in the Lyman- α analysis (see table 3). Along with them, we also varied a set of nuisance parameters which characterize the mass-observable relations:

$$\Theta_{MOR} = \{A_{SZ}, B_{SZ}, C_{SZ}, \sigma_{\ln \zeta}, \rho_{SZ-WL}, \delta_{WL,bias}, \delta_{WL,scatter}, \delta_{Megacam}, \delta_{LSS,Megacam}, \delta_{HST}, \delta_{LSS,HST}\}, \quad (11)$$

where ρ_{SZ-WL} is the correlation coefficient (i.e. the normalized covariance) between the SZ and WL mass proxies; it can assume values

⁴ <https://getdist.readthedocs.io/>

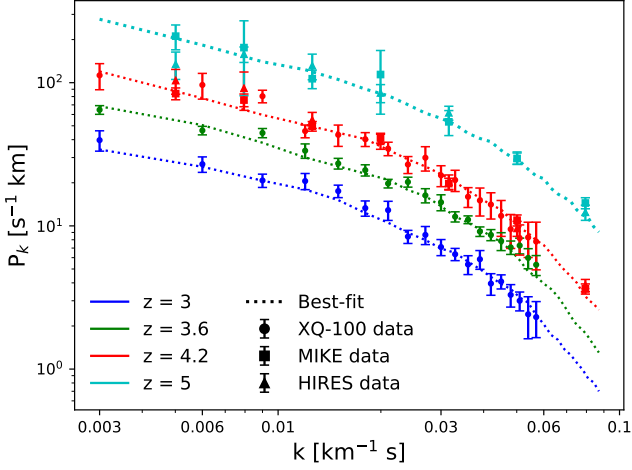


Figure 1. Simulated $P_F(k)$ for the best-fit parameters of our reference Lyman- α analysis for selected redshift bins. Different colors refer to different redshifts, while the shape of the markers indicates which survey each data point belongs to.

in the range $[-1, +1]$, where $\rho_{SZ-WL} > 0$ ($\rho_{SZ-WL} < 0$) indicates that the two random variables are correlated (anti-correlated) and $\rho_{SZ-WL} = 0$ that they are totally uncorrelated.

The original work of B19 also included X-ray Chandra measurements that are used along with the WL data to calibrate the SZ mass-observable relation. These are measurements of $Y_X = M_g T_X$ - where M_g is the gas mass and T_X is the X-ray temperature of the cluster - a typical quantity used in X-ray cluster cosmology (Kravtsov et al. 2006). We decided to not include the Y_X fitting parameters and to restrict our analysis to a calibration through WL data alone. The reason behind this choice is that the inclusion of X-ray data does not improve the constraints on the cosmological parameters and only impacts on the posterior of $\sigma_{\ln \xi}$, as shown in B19 (see their appendix B). Thus, following their approach, we dropped the X-ray mass calibration and instead set a prior on $\sigma_{\ln \xi}$ to speed up convergence. Additionally, we also set Gaussian priors on the free parameters δ , appearing in eqs.(4) and (5), so as to account for the Gaussian distribution of the uncertainties in the systematics Δ of the WL mass modelling. To this purpose, we assume for these δ parameters Gaussian priors with zero mean and unity standard deviation. All the priors on the relevant parameters are reported in table 4. Among the reported uniform priors, the one on ρ_{SZ-WL} spans the full range of possible values, while those on the SZ MOR parameters are set to tighter, yet non-informative, ranges based on previous analyses.

The marginalized contours obtained from the galaxy clusters analysis are shown in fig. 3. The figure shows that the SPT data does not constrain n_s , but as we expected, can constrain well $\Omega_{m,0}$ and σ_8 , pointing to lower values of σ_8 with respect to those obtained in the Lyman- α analysis. Notably, the contours that we obtained for σ_8 are not identical to those published in B19. This is due to the fact that in this analysis we use the "neutrino prescription" (Costanzi et al. 2013) for the HMF i.e. we use the cold dark matter + baryons power spectrum for the computation of the Tinker HMF, in opposition to what is done in B19 in which the total matter power spectrum is used instead. In addition to that, we assume 3 degenerate massive, while in B19 the analysis was based on a single massive neutrino. These differences result in the shift in σ_8 shown in fig. 7 as pointed out in Costanzi et al. (2021) (see their note number 9 for further details).

| Parameter | Prior |
|------------------------|---|
| A_{SZ} | $\mathcal{U}(3, 10)$ |
| B_{SZ} | $\mathcal{U}(1.2, 2)$ |
| C_{SZ} | $\mathcal{U}(-1, 2)$ |
| $\sigma_{\ln \xi}$ | $\mathcal{U}(0.01, 0.5) \times \mathcal{N}(0.13, 0.13)$ |
| ρ_{SZ-WL} | $\mathcal{U}(-1, 1)$ |
| $\delta_{LSS,HST}$ | $\mathcal{U}(-3, 3) \times \mathcal{N}(0, 1)$ |
| $\delta_{WL,bias}$ | $\mathcal{U}(-3, 3) \times \mathcal{N}(0, 1)$ |
| $\delta_{Megacam}$ | $\mathcal{U}(-3, 3) \times \mathcal{N}(0, 1)$ |
| δ_{HST} | $\mathcal{U}(-3, 3) \times \mathcal{N}(0, 1)$ |
| $\delta_{WL,scatter}$ | $\mathcal{U}(-3, 3) \times \mathcal{N}(0, 1)$ |
| $\delta_{LSS,Megacam}$ | $\mathcal{U}(-3, 3) \times \mathcal{N}(0, 1)$ |

Table 4. Priors on the MOR parameter, following those used in the analysis of B19.

To evaluate how well the best-fit model can reproduce the data, we follow the approach used in B19 and evaluate the C-statistics (Cash 1979) instead of the χ^2 , as the latter is not reliable in our case due to the small number of cluster counts within each redshift and ξ (or mass) bin (Kaastra 2017). The (z, ξ) plane sampled by the SPT clusters is divided into 6 evenly spaced z -bins between $z = 0.25$ and $z = 1.75$ and 9 log-spaced ξ -bins between $\xi = 5$ and $\xi = 50$. With this binning, the expected mean C_e and standard deviation C_{std} calculated from the best-fit simulated number counts are⁵:

$$C_e = 39.0 \quad C_{std} = 8.3 \quad (12)$$

Confronting this with the data statistic for our sample,

$$C_d = 62.4, \quad (13)$$

we found a discrepancy between the expected and measured values. We can track down the reason for the bad value of C_d to a particular bin which contains no cluster, despite its expectation value of ~ 7 counts. This is shown in fig. 2 (see the fourth ξ -bin in the second panel from the top) where we show the counts for each of the redshift bins as a function of ξ ⁶. Overall, the agreement is qualitatively good, showing that despite the outlier bin, the model can reproduce the data quite well. Removing this single redshift and mass bin, and evaluating the C-statistic again, gives

$$C_e = 38.0 \quad C_{std} = 8.2 \quad C_d = 48.9, \quad (14)$$

thus supporting the indication that most of the disagreement between the observed SPT cluster counts and the model-predicted ones is due to this single outlier.

4.3 Comparing the cosmological constraints

We have anticipated in the previous sections that the SPT cluster number counts can effectively constrain $\Omega_{m,0}$ and σ_8 , while the HIRES/MIKE and XQ-100 Lyman- α spectra constrain σ_8 and n_s . Therefore, σ_8 is the parameter which is constrained in independent ways by SPT clusters and by Lyman- α data. For this reason, before combining the likelihoods of these two analyses, it is fair to compare the two σ_8 posteriors obtained from the two probes. In fact, we should

⁵ To calculate these values we used the python package CASHSTATISTIC <https://github.com/abmantz/cstat>

⁶ Interestingly, a similar deficit of massive cluster in the redshift bin $0.5 < z < 0.65$ is also observed in the optical DES Y1 redMaPPer catalog, which overlap by $\sim 1300 \text{ deg}^2$ with the SPT SZ survey footprint (see e.g. Fig. 4 in Costanzi et al. 2021).

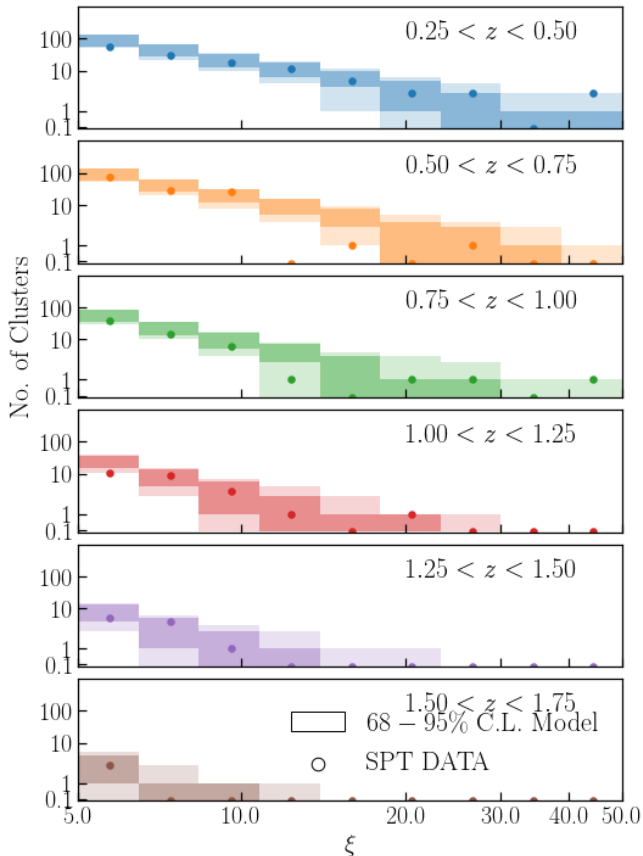


Figure 2. Cluster number counts as a function of the SPT detection significance ξ in 6 different redshift bins. The filled circles represent the SPT cluster number counts, while the shaded areas include the model predictions at the 68 per cent and 95 per cent C.L. The error bars are obtained assuming a Poisson distribution for the predicted counts. The fourth ξ bin at $0.50 < z < 0.75$ shows a strong discrepancy between the observed and the predicted count, raising the value of the C-statistic (see text for details).

| Parameter | Galaxy Clusters | | Lyman- α | |
|---------------------|-----------------|----------|-----------------|----------|
| | 95% C.L. | Best fit | 95% C.L. | Best fit |
| $\Omega_{m,0}$ | [0.21, 0.40] | 0.34 | [0.18, 0.56] | 0.35 |
| A_s [10^{-9}] | [0.80, 4.11] | 1.62 | [1.32, 5.72] | 2.48 |
| n_s | [0.7, 1.0] | 0.91 | [0.7, 1.0] | 0.84 |
| σ_8 | [0.68, 0.81] | 0.74 | [0.84, 0.98] | 0.90 |

Table 5. Marginalized constraints at 95 per cent C.L. obtained from the galaxy clusters, the Lyman- α and the combined analysis, when using informative priors on both cosmological and nuisance parameters (see text). The best-fit values are also shown.

make sure that we are not combining constraints from independent data which are incompatible at a high significance. In that case, the results of the joint analysis must be handled with great care as they might point to erroneous conclusions, singling out a region of the posterior that is not favoured by any of the data sets separately. In table 5 we present the marginalized constraints obtained from the two analyses for the common parameters and we display the relative contours in the triangle plot of fig. 3.

It is clear from fig. 3 that there is a tension on the constraints

on σ_8 , as the contours obtained from the two probes do not overlap. This may be due to some undetected systematics or insufficient modelling of the observations. The tension could also be the signature of the failure of the standard Λ CDM model, which could not be able to provide the connection between the scale- and redshift-ranges over which Lyman- α and SPT clusters probe density perturbations. Clearly, before jumping to this far-reaching conclusion, it is necessary to have a clear understanding of all the possible systematics entering in our analysis.

First of all, we quantify the degree of disagreement between Lyman- α and SPT clusters constraints by following the approach proposed by Bocquet et al. (2019) by using the publicly available code released by these authors⁷. The code calculates the probability distribution of the difference, δ , between pair of points randomly drawn from the two 1D posteriors that are being tested (in our case the σ_8 posteriors). The p-value that the two posteriors trace the same underlying distribution is then evaluated as

$$p = \int_{D < D(0)} d\delta D(\delta), \quad (15)$$

where D is the probability distribution of δ and $D(0)$ is its value for $\delta = 0$. Using this method on the σ_8 marginalized posteriors obtained with the Lyman- α and the SPT analyses, we obtain:

$$p_{\sigma_8} = 0.001, \quad (16)$$

which corresponds to a significance of about 3.3σ under the assumption of Gaussian statistics. This demonstrates that the σ_8 tension between the two probes is quite significant.

Interestingly, we find that despite the tension on σ_8 , the marginalized posteriors on A_s obtained from the two analyses overlap perfectly. This may sound surprising due to the expected correlation between σ_8 and A_s as both these parameters measure the amplitude of the matter power spectrum. However, σ_8 is a measurement of such amplitude extrapolated at $z = 0$ and on a scale of $8 h^{-1} \text{Mpc}$, a scale at which our probes are sensitive. Conversely, A_s represents the primordial amplitude of the matter fluctuations and is constrained by our data only through an extrapolation at large scales of the constraints obtained on the smaller scales directly probed by Lyman- α spectra and SPT clusters. Hence, the mapping between the two has to take into account the other cosmological parameters (namely $\Omega_{m,0}$ and n_s), which have a role in defining the shape of the power spectrum and which are constrained neither by the SPT number counts nor by the HIRES/MIKE and XQ-100 Lyman- α spectra. This freedom in the remaining parameters, allows for large overlapping constraints on A_s , despite the tension on σ_8 . This can be better understood by looking, for instance, at the $A_s - \Omega_{m,0}$ panel in fig. 3, where the contours exhibit a tension at almost 2σ .

Hence, the two data sets show a tension on σ_8 which can be traced to different preferred A_s values, when imposing a strong prior on n_s , e.g. as obtainable from the Planck CMB analyses (e.g. the latest Planck release (Planck Collaboration 2020) gives at the 95% C.L. $n_s = 0.9665 \pm 0.0038$).

4.3.1 Inclusion of the DLA correction

Among all the systematics in the Lyman- α analysis, the one with the largest impact could arise from the incomplete excision of the contamination from damped Lyman- α systems (DLA systems) in the observed quasar spectra. Such strong absorption systems are very rare

⁷ <https://github.com/SebastianBocquet/PosteriorAgreement>

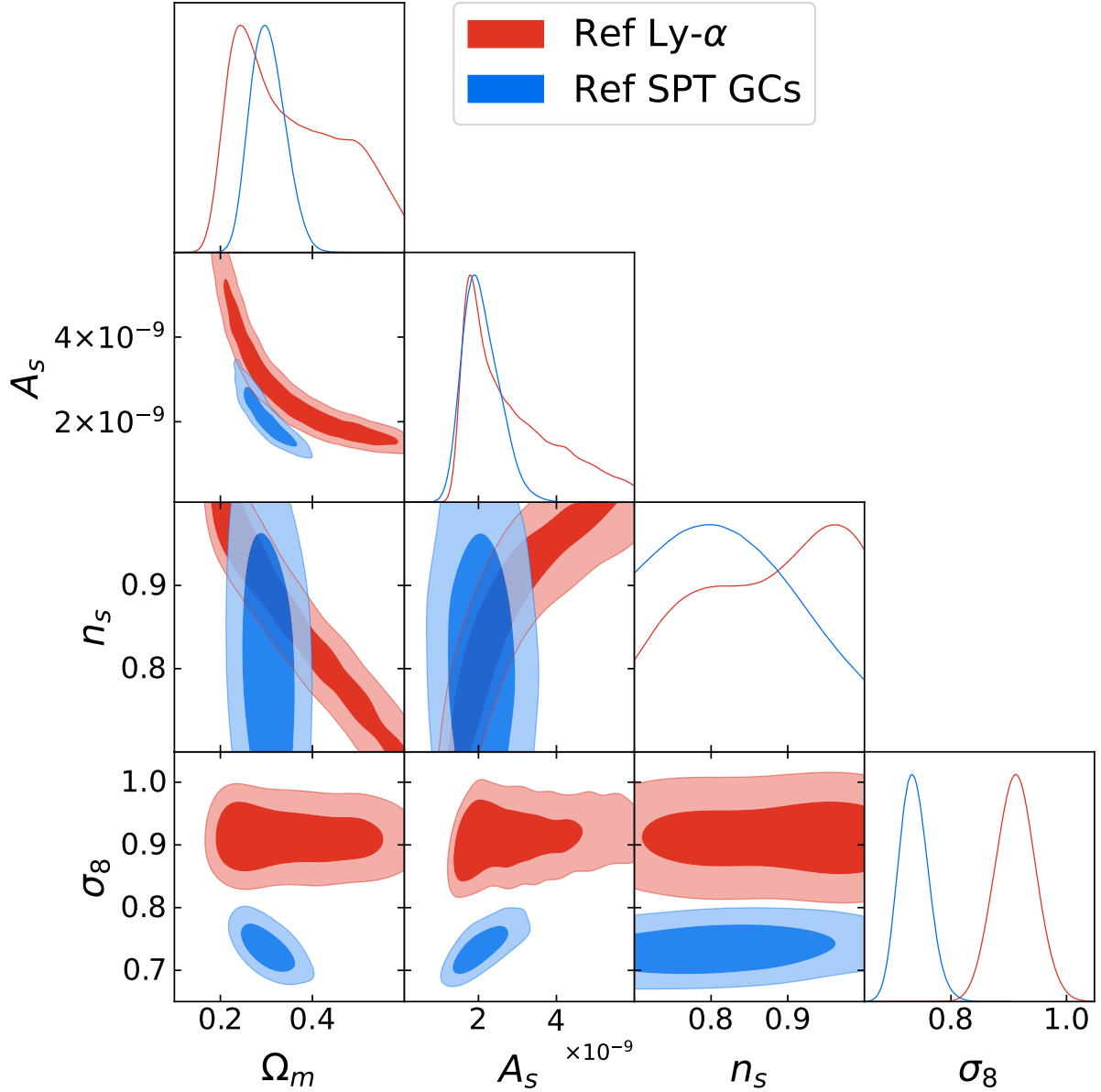


Figure 3. Triangle plot of selected parameters for the chains obtained with the SPT cluster number counts (blue) and the XQ-100 and HIRES/MIKE Lyman- α spectra (red). The marginalized posteriors are plotted only for $\Omega_{m,0}$, A_s , n_s and σ_8 , because these are the parameters effectively constrained by the two data sets. For the other cosmological parameters, the contours only reflect the prior distributions. The filled and shaded areas represent respectively the 68 per cent and 95 per cent C.L. contours.

and should be included by hand in the hydrodynamical simulations when extracting mock quasar spectra from such simulations. To avoid this procedure, the commonly adopted approach is rather to identify and eliminate from the data set those portions of spectra that include strong absorption systems. However, for smaller Hydrogen column densities, e.g. Lyman limits systems (LLS) or subDLAs, it can be quite difficult to identify such systems, thus possibly leading to the introduction of some systematics in the interpretation of the spectra.

Following Rogers et al. (2017), we modelled the residual contributions to the flux power spectrum from LLSs and subDLAs, assuming that all the small and large DLAs have been successfully removed during data reduction. Adopting the same notation as in Rogers et al. (2017) (see Eq. 8 in their paper), we refer to $\alpha_{LLS}(z)$ and $\alpha_{subDLA}(z)$ as the relative contribution fractions to the flux

power spectrum coming from LLSs and subDLAs respectively. We varied these parameters in our chain in two different ways: (i) as redshift independent parameters; (ii) as power-laws of $(1+z)$, varying only the amplitude and fixing the slope to the value obtained by fitting table 1 of Rogers et al. (2017). We point out that the results in terms of cosmological constraints by adopting either one or the other of these two approaches are virtually identical.

The impact of including this correction for strong absorbers (for the case of redshift independent parameters) on the cosmological constraints are shown in fig. 4, where they are compared to the constraints from our reference Lyman- α analysis. Notably, the value preferred for α_{subDLA} is 0, thus suggesting that these systems have been correctly removed from the spectra. Nonetheless, this does not hold for α_{LLS} , so that the correction to the flux power spectrum in-

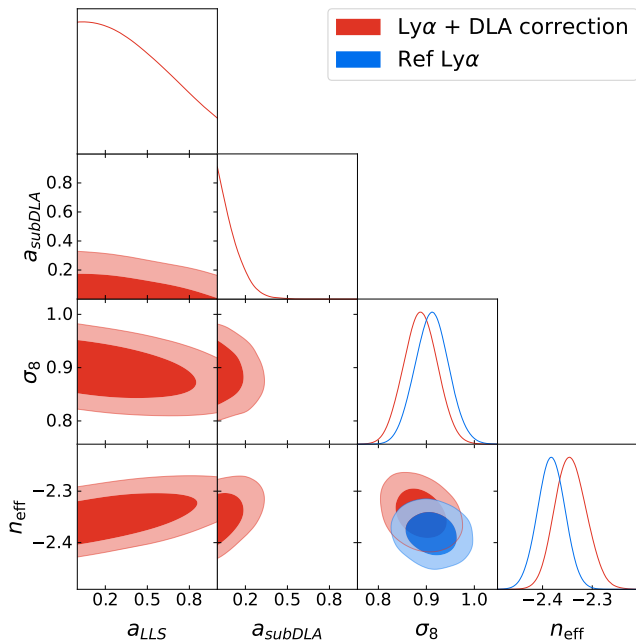


Figure 4. Triangle plot showing the marginalized 1σ and 2σ contours for σ_8 and n_{eff} , as well as for the two DLA correction parameters, for the reference Lyman- α chain and the one with the inclusion of the DLA correction parameters. Varying such parameters reduces the tension with the SPT data, but not significantly.

roduced with this parameter shifts the contours for the cosmological parameters towards slightly lower σ_8 and higher n_{eff} (see table B3 for the full table of constraints). This slightly reduces the tension with the SPT constraints, but only down to 2.8σ .

4.3.2 Interchanging cosmology

As a final test, we further investigate by how much we would need to change the astrophysical parameters of the SPT analysis in order to alleviate the tension with the Lyman- α cosmological constraints, and viceversa. Hence, we took the 4D multivariate posteriors obtained for $\Omega_{m,0}$, A_s , n_s and σ_8 in the reference analyses and used them as priors for two new chains interchanging the cosmology.

Lyman- α analysis with SPT cosmology. When assuming in the Lyman- α analysis the cosmological priors from the analysis of the SPT clusters, we relax any priors on the IGM parameters and let them vary freely. In particular, the mean fluxes at each redshift bin are the IGM parameters that have the strongest correlation with σ_8 and in fact are the ones that are shifted the most, toward lower values.

The shift in the mean fluxes is not as large as that on σ_8 , probably because the tension is in this way spread on more parameters and also because the measurement of σ_8 is quite robust and the low σ_8 value provided by the SPT cosmology prior can only be partially compensated by the other parameters. Confirming this, the χ^2 obtained with this chain is worse ($\Delta[\chi^2] \simeq +4$) with respect to the one obtained with the reference Lyman- α analysis, in spite of an increase in the number of free parameters and thus a decrease in the degree of freedom ($\Delta[\text{d.o.f.}] \simeq -7$).

Nonetheless, even at this level, the mean fluxes constrained with this analysis exhibit a tension with independent measurements (Becker et al. 2013). We show this in fig. 5, where we confront this

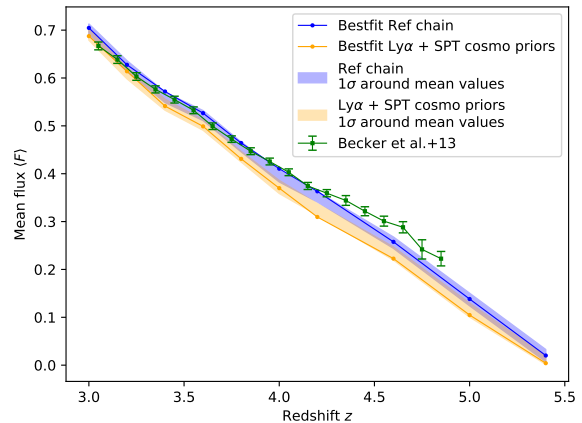


Figure 5. Redshift evolution of the mean fluxes in the bestfit models obtained with the Lyman- α reference analysis and with the analysis with the SPT cosmology. The shaded areas enclose the 1σ region around the mean of the posteriors. The points with error bar are independent measurements published in Becker et al. (2013).

measurements with the predicted mean fluxes evolution with redshift for the Lyman- α reference analysis and for the one with the SPT cosmology. The main uncertainty in determining the mean flux typically resides in the fitting of the continuum of the quasar spectra. Due to large amount of absorption at higher redshifts, this is more of a challenge for MIKE/HIRES data than for XQ-100 or for example BOSS. However, the bias goes in the other direction, such that the mean flux is typically underestimated (Faucher-Giguère et al. 2008; Wilson et al. 2021). Hence, correcting for such a bias would make the tension between the measurements of Becker et al. (2013) and the values inferred in the analysis with fixed lower σ_8 even stronger.

SPT analysis with Lyman- α cosmology. In a similar way, we ran the SPT analysis by using as priors on $\Omega_{m,0}$, A_s , n_s and σ_8 the Gaussian multivariate obtained from the posterior of our reference Lyman- α chain. We did not use the mass calibration adopted in our reference analysis of the SPT cluster counts, and dropped all the priors on the SZ scaling parameters. In this case, the prior on σ_8 is informative enough to have a posterior on this parameter that agrees well with the reference Lyman- α one. To obtain such a large σ_8 value, the SPT data prefer a very low value for the amplitude of the SZ mass-observable relation, A_{SZ} . This in turn means that with the Lyman- α cosmology more massive clusters would correspond to a given SZ signal. We show the SZ scaling relation for the reference SPT analysis and the one with the SPT cosmology in fig. 6. The disagreement between the amplitude of the reference SZ mass-observable relation used in our analysis and that required to bring SPT cluster counts in agreement with Lyman- α cosmology turns out to be at $\sim 3.4\sigma$ when comparing the marginalized posteriors. This highlights that an exceedingly large change in the SZ mass-observable relation should be invoked to reconcile the cosmological parameters preferred by SPT cluster counts and Lyman- α flux power spectrum.

5 SUMMARY AND CONCLUSIONS

We presented a comparison of the constraints on cosmological parameters obtained from the analysis of the SPT cluster number counts

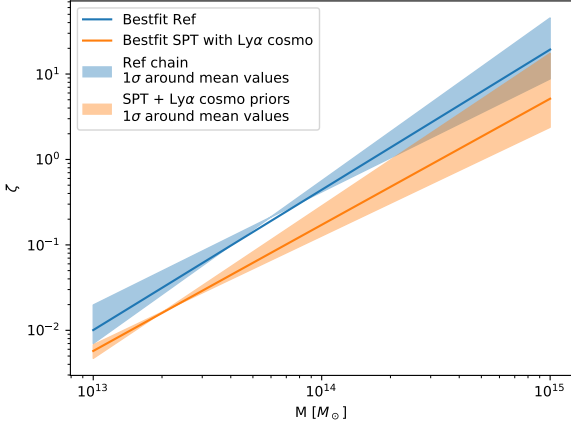


Figure 6. SZ mass scaling relations at the pivot redshift ($z = 0.6$) obtained with the SPT reference analysis and with the analysis with the Lyman- α cosmology. The shaded areas enclose the 1σ region around the mean of the posteriors.

(Bleem et al. 2015) and from the HIRES/MIKE (Viel et al. 2013a) and XQ-100 (López, S. et al. 2016) Lyman- α spectra. These two probes measure the matter power spectrum at complementary scales and over different redshifts ranges. As such, their combination should in principle provide unique constraints on the underlying cosmological model by tracing cosmic growth over more than 90 per cent of cosmic history.

To judge the feasibility of this multiprobe analysis, we first assess possible tensions between the two data sets by comparing their cosmological posteriors. To this end, we employed the publicly available likelihood `CosmoSIS` module described in Bocquet et al. (2019) for the SPT analysis and integrated the likelihood scheme presented in Iršič et al. (2017) in another `CosmoSIS` module for the Lyman- α analysis.

Our main finding in this work is a significant tension in the determination of the amplitude of the linear matter power spectrum, as described by σ_8 , between the value preferred by the SPT cluster number counts and the Lyman- α flux power spectrum:

$$\sigma_8^{\text{GCs}} = 0.738_{-0.040}^{+0.026} \quad \sigma_8^{\text{Ly}\alpha} = 0.911_{-0.035}^{+0.034}. \quad (17)$$

Using the publicly available Python package described in Bocquet et al. (2019), we quantified the degree of disagreement between the two 1D posteriors and found that the two measurements of σ_8 differ at $\approx 3.3\sigma$.

In order to further investigate such tension, we performed a list of different tests varying the parameter space and the priors on such parameters:

- Using independent z-bins instead of a power-law parametrization for the temperature at mean density T_0 in the analysis of the Lyman- α data has a negligible effect on the cosmological posteriors, thus showing the robustness of the σ_8 tension with respect to the choice of different methods in our modelling of the IGM.
- Extending the parameter space of the Lyman- α analysis to include a possible residual contribution from subDLA and LLS that may not have been excised from the data, relaxes the cosmological posteriors and shifts the σ_8 posterior to:

$$\sigma_8^{\text{DLA}} = 0.888_{-0.035}^{+0.035}. \quad (18)$$

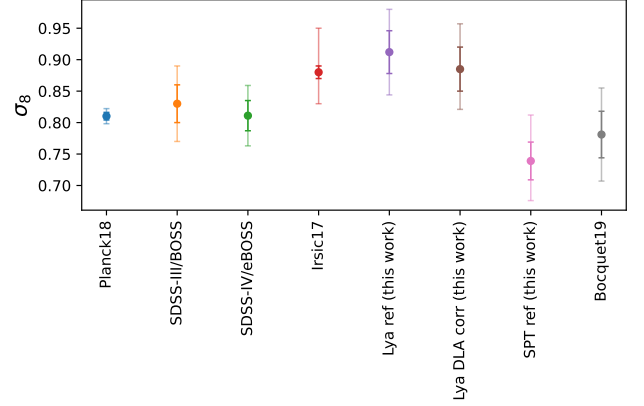


Figure 7. Constraints at 1σ and 2σ level for σ_8 obtained in different analyses. The Planck, SDSS and SPT cluster papers do not report their 2σ constraints, hence for those cases we plot twice the 1σ ones. On the other hand, for I17 and this work's result, we assume gaussian statistic and show the 68% and 95% C.L. as the 1σ and 2σ contours respectively.

This reduces the tension with the SPT results to $\sim 2.8\sigma$. Hence, we conclude that the origin of this tension cannot be due (at least not solely) to the unaccounted effect of DLA systems.

- Analyzing the SPT data adopting the Lyman- α cosmological posteriors as priors, we found that the shift in σ_8 corresponds mainly to a large shift ($\sim 3.4\sigma$) to lower values of the amplitude of the SZ mass-observable relation. Hence, to completely solve the tension the weak lensing mass estimates should be biased low by $\sim 50\%$.
- On the other hand, using the 1σ σ_8 marginalized posterior obtained from the SPT analysis as a prior in the Lyman- α analysis is not informative enough to push the contours to such a low σ_8 value, given the strong constraining power that the Lyman- α data have on such a parameter. Nonetheless, the shift in the σ_8 posterior, drives the Lyman- α analysis to values of the mean fluxes that are in clear tension with independent measurements (Becker et al. 2013). A bias given by continuum fitting is incompatible with such a shift as it typically points to the opposite direction (Faucher-Giguère et al. 2008).

To put things in perspective, we show in fig. 7 the 1σ and 2σ contours obtained using the latest CMB data from Planck (Planck Collaboration 2020), the constraints obtained from the Lyman- α flux power spectrum analyses with SDSS-III (Palanque-Delabrouille et al. 2013) and SDSS-IV (Palanque-Delabrouille et al. 2020) data and those obtained in this work, as well as the constraints in the original analyses of I17 and B19 that we have reproduced. Note that our Lyman- α results differ from those of I17 because we explored a slightly larger parameter space and because the analysis of I17 had an artefact in the interpolation scheme of cosmological parameters that produced artificially stronger 1σ constraints. This however do not affect the 2σ contours which are in agreement with our results (see appendix A for details). Our results for the Lyman- α analysis also show a moderate tension with the BOSS/eBOSS analysis. If our σ_8 measurement is just a statistical fluctuation, then the eBOSS analysis could be averaging out such a feature thanks to the larger number of objects included in the survey (while our analysis only uses ~ 100 spectra, eBOSS has ~ 10000 spectra for the flux power spectrum measurement). On the other hand, given their different nature in terms of number of objects, resolution and SNR the two analyses may be affected by different systematics (continuum fitting and DLA

correction, for example, typically have a stronger effect on larger scales, which are not really sampled by our data; see fig.8 and 9 in [Karaçaylı et al. 2021](#)) or even physical phenomena. At the same time, also the SPT constraints are not identical to those published in [B19](#). The reason for this shift is due to the different prescription used for the halo mass function in the presence of massive neutrinos, as proposed in [Costanzi et al. \(2013\)](#) and applied to the SPT number counts in [Costanzi et al. \(2021\)](#). With respect to previous works, the tension in the determination of σ_8 is stronger when using the XQ-100 and HIRES/MIKE Lyman- α spectra and the SPT cluster number counts. Moreover, the CMB results lie in between the ranges preferred by the analyses performed in this work, also showing a moderate tension of each of them with the Planck data. It is important to mention in the context of the so-called " σ_8 tension" that other LSS probes can constrain this parameter. Some examples are the 3x2 analyses from HSC-Y1 ([Hikage et al. \(2019\)](#)), $\sigma_8 \sim 1.05$), KiDS-1000 ([Heymans et al. \(2021\)](#)), $\sigma_8 \sim 0.76$) and DES-Y3 ([DES Collaboration et al. \(2021\)](#)), $\sigma_8 \sim 0.70$) or the BAO+RSD eBOSS analysis ([Alam et al. \(2021\)](#)), $\sigma_8 \sim 0.81$).

The results of this analysis points towards one or more unmodeled systematics either in the cluster number counts, in the Lyman- α forest spectra or in both probes. The most likely systematics that could have been underestimated in our analysis are the weak lensing mass calibration for the SPT clusters and the continuum fitting and subDLA contribution for the Lyman- α analysis. However, we have shown in this work that these do not seem to be able to compensate the tension on σ_8 unless we assume that such systematics are at a level that can hardly be reconciled with other observational constraints.

Clearly, a more exciting possibility is that this tension signals a deviation from the standard $\nu\Lambda$ CDM paradigm, which is always implicitly assumed in our analysis. It is thus of paramount importance to further investigate the tension. As a first step, extending the analysis to a $\nu\omega$ CDM model will add other degrees of freedom and may (at least partially) relax the tension. Then, more exotic extensions of the standard model could be tested, like for example models with coupled DE-DM, with warm or mixed (cold+warm) DM or scenarios in which the DM is not stable and decays varying its density with time.

The advent of the ESA's Euclid satellite is expected to provide large samples of galaxy clusters identified in the optical/near-IR photometric survey ([Euclid Collaboration et al. 2019](#)). At the same time, the DESI survey will also yield a huge number of QSO spectra over a wide redshift range ([Yèche et al. 2020](#)). This will open up the possibility to carry out similar joint analyses with different and much richer data sets and better understand if this tension is pointing to the need of revising the $\nu\Lambda$ CDM paradigm or is only given by a limited control of the systematics involved in the cosmological analyses of such two complementary probes.

ACKNOWLEDGEMENTS

MV, SB, AS are supported by INFN PD51 INDARK grant. AS and MC are supported by the ERC-StG 'ClustersXCosmo' grant agreement 716762. AS is also supported by the FARE-MIUR grant 'ClustersXEuclid' R165SBKTMA. We thank S. Bocquet for useful discussions. VI is supported by the Kavli Foundation.

DATA AVAILABILITY

The data underlying this article will be shared on reasonable request to the corresponding author.

REFERENCES

- Alam S., et al., 2021, *Phys. Rev. D*, **103**, 083533
- Allen S. W., Evrard A. E., Mantz A. B., 2011, *Annual Review of Astronomy and Astrophysics*, **49**, 409–470
- Becker G. D., Hewett P. C., Worseck G., Prochaska J. X., 2013, *Monthly Notices of the Royal Astronomical Society*, **430**, 2067
- Bleem L. E., et al., 2015, *ApJS*, **216**, 27
- Bocquet S., et al., 2019, *The Astrophysical Journal*, **878**, 55
- Boera E., Becker G. D., Bolton J. S., Nasir F., 2019, *ApJ*, **872**, 101
- Bolton J. S., Viel M., 2011, *Monthly Notices of the Royal Astronomical Society*, **414**, 241
- Bolton J. S., Puchwein E., Sijacki D., Haehnelt M. G., Kim T.-S., Meiksin A., Regan J. A., Viel M., 2016, *Monthly Notices of the Royal Astronomical Society*, **464**, 897
- Borgani S., Viel M., 2009, *MNRAS*, **392**, L26
- Cash W., 1979, *ApJ*, **228**, 939
- Chabanier S., et al., 2019, *J. Cosmology Astropart. Phys.*, **2019**, 017
- Costanzi M., Villaescusa-Navarro F., Viel M., Xia J.-Q., Borgani S., Castorina E., Sefusatti E., 2013, *Journal of Cosmology and Astroparticle Physics*, **2013**, 012–012
- Costanzi M., Sartoris B., Viel M., Borgani S., 2014, *Journal of Cosmology and Astroparticle Physics*, **2014**, 081
- Costanzi M., et al., 2021, *Phys. Rev. D*, **103**, 043522
- DES Collaboration et al., 2021, arXiv e-prints, p. arXiv:2105.13549
- Dietrich J. P., et al., 2019, *MNRAS*, **483**, 2871
- Euclid Collaboration et al., 2019, *A&A*, **627**, A23
- Faucher-Giguère C.-A., Prochaska J. X., Lidz A., Hernquist L., Zaldarriaga M., 2008, *ApJ*, **681**, 831
- Feroz F., Hobson M. P., Bridges M., 2009, *Monthly Notices of the Royal Astronomical Society*, **398**, 1601
- Haardt F., Madau P., 2012, *ApJ*, **746**, 125
- Heymans C., et al., 2021, *Astronomy & Astrophysics*, **646**, A140
- Hikage C., et al., 2019, *PASJ*, **71**, 43
- Hilton M., et al., 2018, *ApJS*, **235**, 20
- Iršič V., et al., 2013, *Journal of Cosmology and Astroparticle Physics*, **2013**, 016
- Iršič V., et al., 2017, *Phys. Rev. D*, **96**, 023522
- Iršič V., et al., 2016, *Monthly Notices of the Royal Astronomical Society*, **466**, 4332
- Kaastra J. S., 2017, *A&A*, **605**, A51
- Karaçaylı N. G., et al., 2021, *Monthly Notices of the Royal Astronomical Society*
- Kravtsov A. V., Borgani S., 2012, *ARA&A*, **50**, 353
- Kravtsov A. V., Vikhlinin A., Nagai D., 2006, *The Astrophysical Journal*, **650**, 128
- Lewis A., 2019, GetDist: a Python package for analysing Monte Carlo samples (arXiv:1910.13970)
- Lewis A., Challinor A., Lasenby A., 2000, *ApJ*, **538**, 473
- López, S. et al., 2016, *A&A*, **594**, A91
- McDonald P., et al., 2005, *The Astrophysical Journal*, **635**, 761–783
- McQuinn M., 2016, *Annual Review of Astronomy and Astrophysics*, **54**, 313
- Palanque-Delabrouille N., et al., 2013, *Astronomy & Astrophysics*, **559**, A85
- Palanque-Delabrouille N., Yèche C., Schöneberg N., Lesgourgues J., Walther M., Chabanier S., Armengaud E., 2020, *Journal of Cosmology and Astroparticle Physics*, **2020**, 038–038
- Pedersen C., Font-Ribera A., Rogers K. K., McDonald P., Peiris H. V., Pontzen A., Slosar A., 2021, *J. Cosmology Astropart. Phys.*, **2021**, 033
- Planck Collaboration 2016, *A&A*, **594**, A27
- Planck Collaboration 2020, *A&A*, **641**, A6
- Rogers K. K., Bird S., Peiris H. V., Pontzen A., Font-Ribera A., Leistedt B., 2017, *Monthly Notices of the Royal Astronomical Society*, **474**, 3032
- Rollinde E., Theuns T., Schaye J., Pâris I., Petitjean P., 2012, *Monthly Notices of the Royal Astronomical Society*, **428**, 540
- Schrabback T., et al., 2018, *MNRAS*, **474**, 2635
- Skilling J., 2004, *AIP Conference Proceedings*, **735**, 395
- Springel V., 2005, *Monthly Notices of the Royal Astronomical Society*, **364**, 1105

Sunyaev R. A., Zeldovich Y. B., 1970, *Comments on Astrophysics and Space Physics*, 2, 66

Tinker J., Kravtsov A. V., Klypin A., Abazajian K., Warren M., Yepes G., Gottlöber S., Holz D. E., 2008, *The Astrophysical Journal*, 688, 709

Vanderlinde K., et al., 2010, *ApJ*, 722, 1180

Viel M., Haehnelt M. G., Springel V., 2004, *MNRAS*, 354, 684

Viel M., Becker G. D., Bolton J. S., Haehnelt M. G., 2013a, *Phys. Rev. D*, 88, 043502

Viel M., Schaye J., Booth C. M., 2013b, *MNRAS*, 429, 1734

Walther M., Oñorbe J., Hennawi J. F., Lukić Z., 2019, *ApJ*, 872, 13

Williamson R., et al., 2011, *ApJ*, 738, 139

Wilson B., Iršič V., McQuinn M., 2021, *Monthly Notices of the Royal Astronomical Society*, 509, 2423

Yèche C., et al., 2020, *Research Notes of the American Astronomical Society*, 4, 179

Zuntz J., et al., 2015, *Astronomy and Computing*, 12, 45

de Salas P., Forero D., Ternes C., Tórtola M., Valle J., 2018, *Physics Letters B*, 782, 633–640

APPENDIX A: CONSISTENCY CHECK FOR THE Lyman- α MODULE

In order to validate our COSMOSIS Lyman- α module, we ran a chain in the same parameter space explored in I17 (i.e. directly varying σ_8 and n_{eff} and fixing the other cosmological parameters to Planck-like values). The results of this analysis are displayed in the triangle plot of fig. A1 for a selection of the varied parameters. We show the contours at 68% and 95% C.L. and compare them with the results in I17. The main difference between the two analyses resides in an artefact in the interpolation scheme that has been fixed in this new analysis. In practice, this produced artificially tight constraints at the 68% confidence level in I17, but did not affect them at the 95% confidence level. Moreover, our analysis extends the range of $\langle F \rangle$ values explored in the chain, giving more freedom also in the determination of the other parameters and allowing, for example, the shift seen in $\langle F \rangle (z=4.2)$.

Another relevant difference between the two analyses resides in the sampling method: while their work is based on a Metropolis-Hastings algorithm, we performed the analysis with a nested sampler. The posteriors have a good qualitative agreement, showing that our pipeline is working properly. Some discrepancy is seen on secondary peaks, due to different starting points or to the different criteria used by the algorithms to determine the number of burn-in samples: in the Metropolis-Hastings algorithm the number of burn-in samples is defined by the user, while in MULTINEST the iteration is terminated when the evaluation of the Bayesian evidence reaches a certain accuracy.

APPENDIX B: BESTFIT AND CONFIDENCE LEVELS TABLES

We present in this section the 1 and 2σ confidence intervals along with the bestfit values for all the parameters varied in the reference SPT and Lyman- α analysis and in the Lyman- α + DLA correction one. The unconstrained cosmological parameters, i.e. h , $\Omega_b h^2$, and $\Omega_{\nu,0} h^2$ have been omitted because the posteriors on those parameters in all the analyses simply reflect the priors.

This paper has been typeset from a $\text{\TeX}/\text{\LaTeX}$ file prepared by the author.

| Parameter | 68% C.L. | 95% C.L. | Best fit |
|----------------------|--------------|--------------|----------|
| A_{SZ} | [5.13, 6.72] | [4.36, 7.71] | 6.38 |
| B_{SZ} | [1.49, 1.63] | [1.41, 1.71] | 1.51 |
| C_{SZ} | [0.55, 1.07] | [0.25, 1.26] | 1.04 |
| $\sigma_{\ln \zeta}$ | [0.10, 0.22] | [0.04, 0.29] | 0.17 |
| Ω_m | [0.26, 0.33] | [0.24, 0.38] | 0.34 |
| $A_s [10^{-9}]$ | [1.52, 2.44] | [1.24, 3.04] | 1.68 |
| n_s | [0.72, 0.89] | [0.70, 1.00] | 0.72 |
| σ_8 | [0.71, 0.76] | [0.69, 0.79] | 0.70 |

Table B1. Marginalized contours at 68% and 95% C.L. as well as bestfit values for the parameters of our reference SPT cluster analysis.

| Parameter | 68% C.L. | 95% C.L. | Best fit |
|------------------|----------------|----------------|----------|
| $F(z=3.0)$ | [0.69, 0.71] | [0.68, 0.72] | 0.70 |
| $F(z=3.2)$ | [0.61, 0.64] | [0.60, 0.65] | 0.63 |
| $F(z=3.4)$ | [0.55, 0.57] | [0.54, 0.58] | 0.57 |
| $F(z=3.6)$ | [0.51, 0.53] | [0.50, 0.54] | 0.53 |
| $F(z=3.8)$ | [0.45, 0.47] | [0.44, 0.48] | 0.46 |
| $F(z=4.0)$ | [0.38, 0.41] | [0.37, 0.42] | 0.41 |
| $F(z=4.2)$ | [0.34, 0.36] | [0.33, 0.37] | 0.36 |
| $F(z=4.6)$ | [0.24, 0.27] | [0.23, 0.28] | 0.26 |
| $F(z=5.0)$ | [0.12, 0.15] | [0.11, 0.16] | 0.14 |
| $F(z=5.4)$ | [0.00, 0.03] | [0.00, 0.04] | 0.02 |
| $T_0^A [10^4 K]$ | [0.86, 1.07] | [0.83, 1.23] | 1.28 |
| T_0^S | [-2.37, -1.15] | [-2.73, -0.45] | -0.93 |
| γ^A | [1.51, 1.70] | [1.37, 1.70] | 1.42 |
| γ^S | [0.79, 1.53] | [0.35, 1.80] | 1.00 |
| f_{QSO} | [0.00, 1.00] | [0.00, 1.00] | 0.50 |
| z_{rei} | [7.85, 12.57] | [6.87, 14.61] | 7.20 |
| n_{eff} | [-2.41, -2.36] | [-2.44, -2.33] | -2.41 |
| Ω_m | [0.21, 0.45] | [0.18, 0.57] | 0.35 |
| $A_s [10^{-9}]$ | [1.37, 3.76] | [0.95, 5.87] | 2.48 |
| n_s | [0.82, 1.00] | [0.70, 1.00] | 0.84 |
| σ_8 | [0.88, 0.95] | [0.84, 0.98] | 0.90 |

Table B2. Marginalized contours at 68% and 95% C.L. as well as bestfit values for the parameters of our reference Lyman- α spectra analysis.

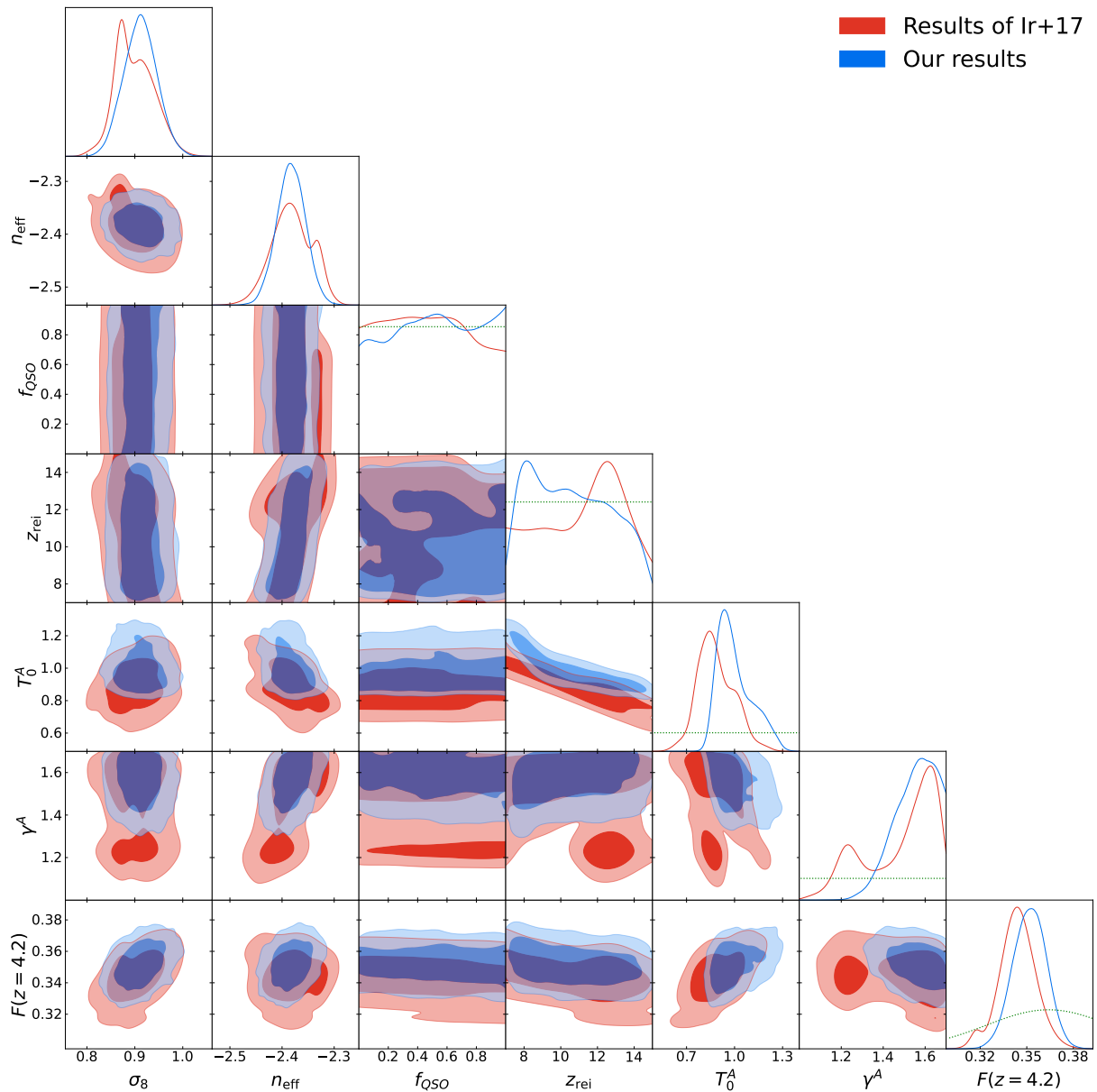


Figure A1. Comparison of the marginalized posteriors obtained with our `CosmosIS` module and those reported in [I17](#) for a selection of parameters. As the redshift pivot of the power-law relations is $z_p = 4.2$, $\gamma(z = 4.2)$ and $T_0(z = 4.2)$ are simply the amplitudes γ^A and T_0^A of the power-law parametrizations. The filled and shaded areas represent respectively the 68% and 95% C.L. contours. The green dotted lines represent the priors used for the varied parameters. No prior is shown in the σ_8 and n_{eff} panels because these are derived parameters.

| Parameter | 68% C.L. | 95% C.L. | Best fit |
|------------------|----------------|----------------|----------|
| $F(z = 3.0)$ | [0.70, 0.72] | [0.69, 0.73] | 0.72 |
| $F(z = 3.2)$ | [0.62, 0.65] | [0.61, 0.66] | 0.64 |
| $F(z = 3.4)$ | [0.56, 0.58] | [0.55, 0.59] | 0.56 |
| $F(z = 3.6)$ | [0.52, 0.54] | [0.51, 0.55] | 0.53 |
| $F(z = 3.8)$ | [0.45, 0.47] | [0.44, 0.48] | 0.46 |
| $F(z = 4.0)$ | [0.39, 0.41] | [0.38, 0.43] | 0.40 |
| $F(z = 4.2)$ | [0.35, 0.37] | [0.34, 0.38] | 0.35 |
| $F(z = 4.6)$ | [0.25, 0.27] | [0.24, 0.28] | 0.25 |
| $F(z = 5.0)$ | [0.13, 0.15] | [0.11, 0.16] | 0.13 |
| $F(z = 5.4)$ | [0.00, 0.03] | [0.00, 0.04] | 0.02 |
| $T_0^A [10^4 K]$ | [0.86, 1.03] | [0.82, 1.20] | 0.88 |
| T_0^S | [-2.30, -1.11] | [-2.64, -0.36] | -2.53 |
| γ^A | [1.56, 1.70] | [1.43, 1.70] | 1.56 |
| γ^S | [0.87, 1.63] | [0.41, 1.86] | 1.67 |
| f_{QSO} | [0.00, 1.00] | [0.00, 1.00] | 0.82 |
| z_{rei} | [8.91, 13.65] | [7.32, 14.79] | 14.62 |
| n_{eff} | [-2.38, -2.31] | [-2.40, -2.28] | -2.34 |
| a_{LLS} | [0.00, 0.54] | [0.00, 1.00] | 0.45 |
| a_{subDLA} | [0.00, 0.12] | [0.00, 0.27] | 0.03 |
| Ω_m | [0.26, 0.50] | [0.24, 0.60] | 0.33 |
| $A_s [10^{-9}]$ | [1.31, 2.69] | [1.01, 4.05] | 2.34 |
| n_s | [0.83, 1.00] | [0.75, 1.00] | 0.91 |
| σ_8 | [0.85, 0.92] | [0.82, 0.96] | 0.89 |

Table B3. Marginalized contours at 68% and 95% C.L. as well as bestfit values for the parameters of our Lyman- α + DLA correction analysis.